Research Article

Yousaf Khan*, Uzma Sharafat, Saima Gul, M. I. Khan*, Muhammad Ismail*, Murad Ali Khan, Rafia Younus, and Sher Bahadar Khan

Novel *in situ* synthesis of quaternary core–shell metallic sulfide nanocomposites for degradation of organic dyes and hydrogen production

https://doi.org/10.1515/gps-2022-8128
received October 15, 2022; accepted March 07, 2023

Abstract: Environmental remediation of toxic organic pollutants on catalytic degradation has gained much attention. Organic dyes and fossil fuels as pollutants are the two major problems nowadays. The efficient and targeted eradication of organic dye from water systems is a critical global concern for the treatment of both drinking water and wastewater. In this study, ZnO–ZnS–CdO–CdS quaternary core–shell nanocomposites (NCs) were synthesized using *Ricinus communis* as a stabilizing agent and hydrazine hydrate as a reducing agent. UV-visible spectroscopy and photoluminescence confirmed the formation of NCs. Fourier transform infrared spectroscopy confirmed the presence of functional groups, while scanning electron microscopy analysis revealed that the morphology of nanomaterials was spherical and poly distributed. X-ray powder diffraction confirmed the crystalline nature of prepared samples. The prepared nanocatalysts were used in the production of hydrogen gas from green sources of the *Brassica campestris* leaf extract and the degradation of Congo red and methyl red dyes. Overall, the photocatalytic performance of NCs and their design was successful. The prepared catalysts were not only active in the degradation of a single substrate but also in the degradation of a mixture of dyes.

Keywords: precipitation method, green synthesis, organic pollutants, hydrogen gas, *Brassica campestris*

1 Introduction

Environmental pollution, particularly water pollution, is increasing with each passing day as a result of massive industrial growth. Textile dyes, pharmaceutical metabolites, and discrete organic solvents make up the majority of industrial waste [1]. Large numbers of industrial effluents are poisonous, non-biodegradable, and harmful to living things. The accumulation of these contaminants in wastewater, particularly organic dyes, can cause both acute and chronic health problems [2,3].

Organic dyes are commonly used in the textile, printing, cosmetic, painting, baking, and plastic industries, as well as in acid–base titration and biological research as indicators and tracers [4]. During the coloring process, the textile and paint industries discharge a large number of organic dyes into wastewater [5]. Among the different dyes used in various industries, azo dyes are regarded to be the largest group of synthetic organic dyes. Because of the azo groups, azo dyes are exceptionally stable [6,7]. More than 2,000 different azo dyes in various natures and forms are in use, with about 1 million tons of planned global azo dye production per year [8,9]. During the painting and synthesizing process, 10–15% of dyes were nearly released into the wastewater. This wastewater containing colors raises concerns about public health and also disrupts aquatic life by lowering gas solubility and light penetration, thereby impacting phytoplankton photosynthetic activities [8,9]. At present, dyes are produced and used widely in many different industries, including printing,

* **Corresponding author: Yousaf Khan,** Department of Chemistry, Kohat University of Science and Technology, Kohat 26000, Khyber Pakhtunkhwa, Pakistan, e-mail: yousafdawar1@gmail.com
* **Corresponding author: M. I. Khan,** Department of Chemistry, Kohat University of Science and Technology, Kohat 26000, Khyber Pakhtunkhwa, Pakistan, e-mail: gorikhan@hotmail.com
* **Corresponding author: Muhammad Ismail,** Department of Chemistry, Kohat University of Science and Technology, Kohat 26000, Khyber Pakhtunkhwa, Pakistan, e-mail: ismailkust@yahoo.com
Uzma Sharafat: School of Science and the Environment, Grenfell Campus, Memorial University of Newfoundland and Labrador, Corner Brook, NL A2H 5G4, Canada
Saima Gul, Murad Ali Khan: Department of Chemistry, Kohat University of Science and Technology, Kohat 26000, Khyber Pakhtunkhwa, Pakistan
Rafia Younus: Department of Environmental Sciences, Gomal University, Dera Ismail Khan, Khyber Pakhtunkhwa, Pakistan
Sher Bahadar Khan: Chemistry Department, Faculty of Science, King Abdulaziz University, P. O. Box 80203, Jeddah 21589, Saudi Arabia

garments, paper and pulp, etc. However, large amounts of dyestuffs are discharged into aqueous habitats, endangering both human health and aquatic life [10]. As a result, wastewater containing industrial dyes must be cleaned using modern procedures before being discharged into the aquatic environment. Metallic nanoparticles (NPs) and nanocomposites (NCs) have been used as excellent photo-catalysts for the removal of organic dyes due to their distinctive localized surface plasmon resonance, increased surface area, and OH^- generation. As a result, it is necessary to eliminate or convert these toxic contaminants into non-poisonous forms [11]. Adsorption, coagulation–flocculation, reverse osmosis, and oxidation are common wastewater treatment methods used, which are less effective for this purpose. Such processes turn dissolved pollutants into solid trash, which can then be released into the environment in one or the other form [12,13]. In this case, the photo-catalysis procedure has been shown to be quite effective in removing such dyes. The presence of a free electron–hole pair in photo-catalysis can generate free radical ($OH^{\cdot}$) species with advanced oxidation properties, which can lead to the complete breakdown of organic pollutants into mineral acids, CO_2, and H_2O [14].

In recent years, in order to achieve long-term industrial benefits, there is a demand for a tremendous increase in clean and green energy production. An environmentally friendly, renewable, and green energy source can help not only to reduce environmental issues but also to alleviate the global energy crisis that is on the horizon. Recently, hydrogen production has received a lot of attention. However, during industrial hydrogen production, a lot of fossil fuels are wasted, resulting in large amounts of NO_x and CO_2 emissions, which are the main causes of the greenhouse effect and industrial smog. The use of photo-catalysts for hydrogen fuel production from green sources can solve this problem because it is a renewable, abundant, clean, and green sources of electricity [15].

The development of suitable photo-catalysts is a key research topic to attain higher photo-catalytic activity. Various types of photo-catalysts have been documented. Metal sulfides and semiconductor NPs, particularly those in groups II–VI, are noteworthy in this regard due to their outstanding chemical and physical features [16]. Generally, researchers are concerned not only with the nanocrystals, structural features, such as crystallography, composition, morphology, and mean size, but also with their surfaces, because nanostructures' surfaces contain a wide range of atoms, the electronic states formed on their surfaces may be critical, influencing the physical properties of the nanostructures. Coating nano-crystals with a shell of an unusual species is one of the strategies for influencing their surface features [17]. Zinc oxide (ZnO), zinc sulfide (ZnS), cadmium oxide (CdO), and cadmium sulfide (CdS) NPs are essential semiconductors in this regard. At room temperature, ZnO has a band gap of 3.7 eV. Solar cells, light-emitting diodes (LED), gas sensors, and field emission are only a few of the technological applications [18]. Similarly, the band gap of ZnS is 3.3 eV, which is sufficient. ZnS has unique properties, such as resistance to high electric fields, large band-gap strength, and photo- and electroluminescence residents. UV LED, infrared purple windows, solar cells, sensors, bio-catalysis, and imaging are only a few of the applications of ZnS [19]. CdO has a band gap of ~2.7 eV, making it a good candidate for photo-catalytic research when combined with other NPs from this group [20]. The band gap of CdS is 2.42 eV and due to its unique properties, CdS NPs have a wide range of applications, including solar cells, LED, photo-catalysis, and optical instruments [21].

Because of excellent optical characteristics, ZnO and ZnS nanomaterials have been extensively employed as photo-catalysts [22]. They are, however, only active in UV light. As a result, attempts have been made to make them active in the visible zone in order to make the best use of solar energy [23]. On the other hand, CdS is an excellent visible light photo-catalyst but it has poor quantum performance due to low stability charge recombination in solution. As a result, significant attempts have been made to increase the photo-catalytic stability of CdS, despite its relatively high photoactivity [24]. Controlling morphology, modifying the structural surface of CdS NPs, doping transition metal ions with CdS [25], applying CdS to graphene sheets or carbon nanotubes to obtain homogeneously allotted CdS QDs [26], and combining CdS with other semiconductors [27] are some of the methods used. In the foregoing attempts, a combination of various band gap semiconductors generating a continuous chain of electron–hole pair is accomplished. So, due to their optoelectronic and structural properties, ZnO, ZnS, and CdO NPs are good semiconductor materials for CdS, forming a series of chains of electron–hole pairs, where their efficiency is increasing [24]. The various methods used for the synthesis include precipitation, solvothermal, hydrothermal, co-precipitation, sol–gel, microwave-aided, and sono-chemical techniques. Over the other approaches, precipitation methods have a distinct advantage since it is easy, inexpensive, and more energetic [28,29]. Here, the successful fabrication of ZnO–ZnS–CdO–CdS core–shell quaternary NCs was demonstrated by using a novel method of chemical precipitation at 80°C.

Despite its low energy density and significant moisture content, biomass offers a potential sustainable fuel source for the production of H_2. However, a number of processes, including gasification, pyrolysis, and super-/subcritical hydrothermal treatment, have been developed to efficiently convert biomass to hydrogen [30,31]. In this study, the prepared nanocatalysts were used in the production of hydrogen gas from green sources of the *Brassica campestris* leaf extract and the degradation of Congo red (CR) and methyl red (MR) dyes.

2 Experimental

2.1 Materials

The chemicals, zinc sulfate heptahydrate ($ZnSO_4{\cdot}7H_2O$), cadmium sulfate octahydrate ($CdSO_4{\cdot}8H_2O$), sodium sulfide (Na_2S), and potassium hydroxide (KOH), were purchased from BDH Chemicals, England. Castor (*Ricinus communis*) oil was purchased from a local Kohat market and used as a capping agent. Hydrazine monohydrate was purchased from Daejung, Korea. Azo dyes, CR, MR, and methyl orange, were from Merck.

2.2 Synthesis of quaternary ZnO–ZnS–CdO–CdS NCs

First, 50 mL of 0.05 M aqueous $ZnSO_4{\cdot}7H_2O$ was taken in a round bottom flask and stirred with a magnetic stirrer. The capping agent solution was prepared by dissolving 1 mL of castor oil in 10 mL of absolute ethanol. Then, the castor oil solution was added dropwise in a round bottom flask containing zinc sulfate solution and mixed. For the synthesis of ZnO, 1 mL of hydrazine monohydrate was added dropwise to the zinc sulfate solution and mixed continuously with a magnetic stirrer until white precipitates were obtained. The formation of white precipitate confirmed the synthesis of ZnO NPs. After washing three times with distilled water, precipitates were suspended in 50 mL of distilled water.

In the second step, 50 mL of 0.05 M aqueous $ZnSO_4{\cdot}7H_2O$ was added to the ZnO suspension. Then, 50 mL of 0.05 M sodium sulfide pentahydrate and 5 mL of ethanolic castor oil were added dropwise. After that, 1 mL of hydrazine monohydrate was added dropwise and stirred until turbid white precipitates were obtained, which confirmed the formation of ZnO–ZnS NCs. The product was washed with distilled water, filtered, and suspended in 50 mL of distilled water.

The same experimental procedures were followed for the synthesis of ternary ZnO–ZnS–CdO and quaternary ZnO–ZnS–CdO–CdS NCs using $CdSO_4{\cdot}8H_2O$ as a precursor of cadmium. The NCs were washed with distilled water, followed by washing with ethanol, then dried, and calcined in a furnace at 300°C for 2 h, and stored for future use.

2.3 Photo-catalytic degradation of dyes

Organic dyes CR and MR degradation were carried out using synthesized NCs. First, 50 mL of 0.04 mM dye solution was taken in a round bottom flask, and its spectra were recorded using a UV-visible (UV-Vis) spectrophotometer in a quartz cuvette. Then, 50 mg of NCs was added and kept in the dark for 5 min to allow the system to reach equilibrium. Then, the reaction mixture in the flask was placed under the solar light and stirred. The spectra of the same solution were then recorded using a UV-Vis spectrophotometer at different time intervals. During the test, the dye concentrations were kept constant at 0.04 mM. The maximum drop in λ_{max} was recorded at 500 nm for CR and 490 nm for MR. The following equation was used to compute the % degradation of the degraded dye:

$$\text{Degradation (\%)} = 100 - \frac{(A_t \times 100)}{A_0} \quad (1)$$

where the starting absorbance is denoted by A_0 and the absorbance at different time intervals is represented by A_t.

2.4 Gas generation from the biomass

The biomass of *Brassica campestris* leaves was collected and dried at room temperature. The leaves were then pulverized into powder. Following that, 6 g of the leaf powder was dissolved in 0.05 M aqueous KOH solution. The extract was filtered through filter paper after 1 h. The production of gas (H_2) from the biomass was carried out in a round bottom flask as a reaction vessel. Reactions were carried out both with and without a catalyst. In the presence of the catalyst, a specific amount of biomass was placed in a round-bottom flask and stirred using a magnetic stirrer. The flask was connected to a 500 mL graduated cylinder through a pipe. The entire reaction was carried out in the light (100 W tungsten lamp). After a few minutes, the generated gas started to cause a drop in the water level in the graduated cylinder.

The amount of the alkaline biomass solution used in the experiment ranged from 10 to 50 mL, while the amount of the catalyst used ranged from 10 to 50 mg.

2.5 Characterization

A UV-Vis spectrophotometer (Shimadzu, UV-1800), with a wavelength range of 200–700 nm was used for optical absorption spectrum monitoring of ZnO–ZnS–CdO–CdS NCs. The photo-catalytic degradation analysis of the organic dyes was also performed using the same apparatus. A NICOLET iS50 Fourier transform infrared (FTIR) spectrophotometer was used to determine the different functional groups that act as stabilizers on the surface of NCs. Average crystalline structures of NPs were analyzed using powder X-ray diffraction (XRD) with a PAN (JDX-3532 JEOL, Japan) analytical diffractometer. An energy dispersive X-ray spectrometer (EDX) 6490 (LA) linked to a MIRA3-TESCAN scanning electron microscope (SEM) was used to examine the elemental composition of the prepared NCs. The DV 420_OE model was used to study the photoluminescence (PL).

3 Results and discussion

3.1 Synthesis of quaternary core–shell NCs

The synthesis of NPs and ZnO–ZnS–CdO–CdS NCs is presented in Figure 1. The formation of white precipitates (Figure A1 in Appendix) after mixing zinc sulfate with hydrazine hydrate confirmed the synthesis of ZnO NPs. Similarly, the formation of turbid white precipitates confirmed the formation of ZnO–ZnS NCs (Figure A1). The product was washed with distilled water, filtered, and suspended in 50 mL of distilled water. The chemical procedure for the configuration of ZnS and CdS NPs is as follows:

$$Na_2S + H_2O + \Delta \rightarrow 2Na^+ + S^-$$

$$S^{2-} + Cd^{2+} \rightarrow CdS$$

$$S^{2-} + Zn^{2+} \rightarrow ZnS$$

In the first phase, sodium sulfide was converted to hydrogen sulfide, which then interacted with Cd^{2+} and Zn^{2+} to form CdS and ZnS, respectively. A pictorial representation is shown in Figure A1.

3.2 Characterization

3.2.1 UV-Vis analysis

The UV-Vis spectra of the prepared NPs and NC samples were recorded using a UV-Vis spectrophotometer. The UV-Vis spectra of the prepared samples are presented in Figure 2a.

The ZnO NPs showed a broad absorption band at around 280 nm. CdO NPs showed an absorption band at 285 nm and a small peak around 305–315 nm [32]. A small peak was observed in ZnS NPs near 280 nm. CdS NPs displayed an absorption band at 440 nm. The oil NCs displayed an absorption band at 420 nm, which indicated

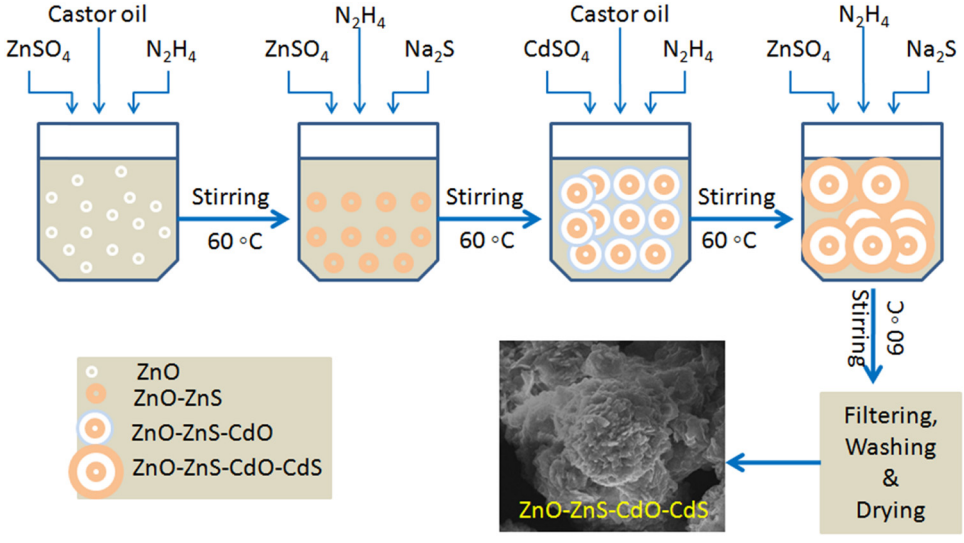

Figure 1: Schematic representation of the NC synthesis.

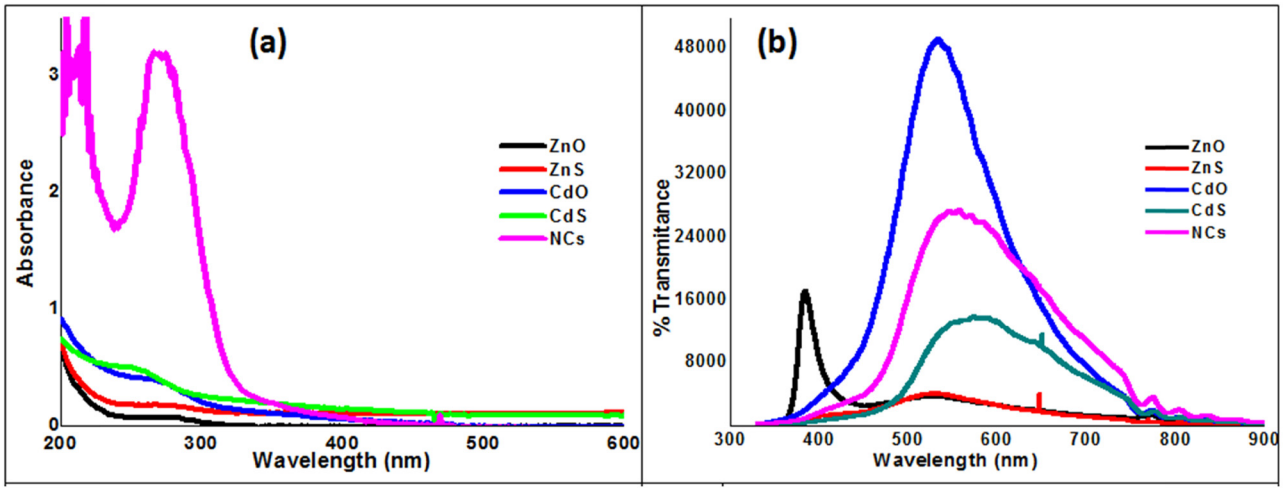

Figure 2: (a) UV-Vis and (b) PL of the synthesized NPs and NCs.

a blue shift in comparison to pure CdS NPs due to quantum confinement. The above absorption bands confirm the configuration of ZnO, ZnS, CdO, CdS NPs, and ZnO–ZnS–CdO–CdS NCs [27,28,33].

3.2.2 PL study

PL spectroscopy is an influential tool to calculate approximately the recombination of photo-induced charge carriers (e^- and h^+). PL not only explains the dependence of photocatalytic activity but also on the transfer rate and separation efficiency of the photo-generated charges as well as improved surface chemistry characteristics of the photo-catalyst [34]. The PL spectra of the prepared NCs were recorded at room temperature in order to examine the optical properties. The electronic structure of the semiconductor nanomaterials may be very clearly seen in the PL spectra [35]. Thus, PL spectra are also very helpful in demonstrating the effective growth of ZnO, and also later the ZnS, CdO, and CdS shells on ZnO NPs to synthesize ZnO–ZnS–CdO–CdS NCs. Figure 2b displays the visible room-temperature PL spectra of ZnO–ZnS–CdO–CdS NCs [36,37].

3.2.3 FT-IR analysis of nanomaterials

Figure 3 shows the FT-IR spectra of the synthesized NPs and NCs, which demonstrate distinct peaks of the functional groups included in the stabilizer in the region

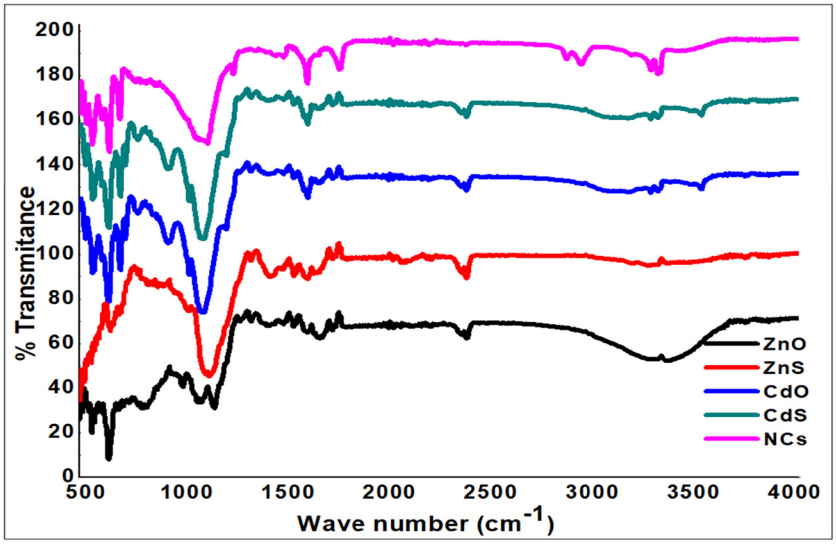

Figure 3: FTIR spectra of the synthesized NPs and NCs.

500–3,500 cm^{-1}. The O–H vibration of stretching is visible in the sharp band between 3,200 and 3,600 cm^{-1} [38,39]. The C–H group stretching vibration has a peak at 2,900–3,100 cm^{-1}. The R–N═C═S bonding is visible on the peaks from 2,086 to 2,093 cm^{-1} [40]. The peaks ranging from 1,009 to 1,150 cm^{-1} indicate stretching vibrations of C–O and C–N, whereas peaks at 1,220 and 1,140 cm^{-1} exhibited bending vibrations of aliphatic amines, respectively. The peaks between 600 and 800 cm^{-1} are attributed to the formation of ZnS and CdS. Furthermore, zinc and CdO vibrations were found to have high peaks at 600 and 500 cm^{-1}, respectively [41–43]. Thus, from the above discussion, it can be concluded that biomolecules of castor oil (organic acids) serve as a stabilizing agent for the prepared nanomaterials.

3.2.4 XRD patterns of nanomaterials

Figure 3 shows the XRD patterns of prepared ZnO, ZnS, CdO, CdS NPs, and ZnO–ZnS–CdO–CdS NCs. It showed the main characteristic peaks with indices of 31.28 (101), 33.88 (002), 48.18 (102), and 63.88 (103), indicating that ZnO NPs had a hexagonal structure [44]. Similarly, major peaks with indices of 28.31 (111), 47.69 (220), and 56.69 (311) were identified, confirming the cubic zinc-blended structure of ZnS NPs [45,46]. Similarly, key feature peaks with indices of 33.37 (111), 38.8 (200), and 55.88 (220) are shown, indicating the cubic structure of CdO [47]. The [111], [220], and [311] diffraction peaks, indicative of the CdS cubic system [48], are also validated in Figure 4.

A mixed structure of ZnO–ZnS–CdO–CdS composites was synthesized, as shown in Figure 4. This validated the hexagonal structure of ZnO and the cubic structures of ZnS, CdO, and CdS, which were unaffected by the coating methods [49]. The Debye–Scherer formula, $L = k\lambda/\beta \frac{1}{2}\cos\theta$, was used to calculate the size of nanocrystallites [50], where θ is the Bragg angle, and λ =1.5418 Å is the X-ray wavelength (Cu source utilized), $\beta = 1/2$ is the full width at half-maximum (FWHM) on a 2θ scale, and k is constant nearly equal to unity. According to Scherer's equation, the average crystallite sizes of ZnO, ZnS, CdO, CdS NPs, and ZnO–ZnS–CdO–CdS NCs were 3, 3.87, 2.96, 3, and 4.72 nm, respectively.

3.2.5 EDX and SEM analyses of nanomaterials

Through energy dispersive X-ray analysis elemental compositions of ZnO NPs, ZnS NPs, CdO NPs, CdS NPs, and ZnO–ZnS–CdO–CdS NPs using castor oil as a catalyst were determined and are shown in Figure 5. The spectra revealed fine signals for Cd and O in CdO, Cd and S in CdS, Zn and O in ZnO, Zn and S in ZnS, and Zn, CdO, and S in ZnO–ZnS–CdO–CdS NPs, demonstrating the reduction of Zn^{2+} into ZnO and ZnS nanomaterials and Cd^{2+} into CdO and CdS nanomaterials. EDX examination revealed the presence of Zn, Cd, O, and S in the formed NPs and NCs [51].

SEM was used to examine the morphology and agglomerated sizes of ZnO, ZnS, CdO, CdS NPs, and ZnO–ZnS–CdO–CdS NCs produced with castor oil, as shown in Figure 6.

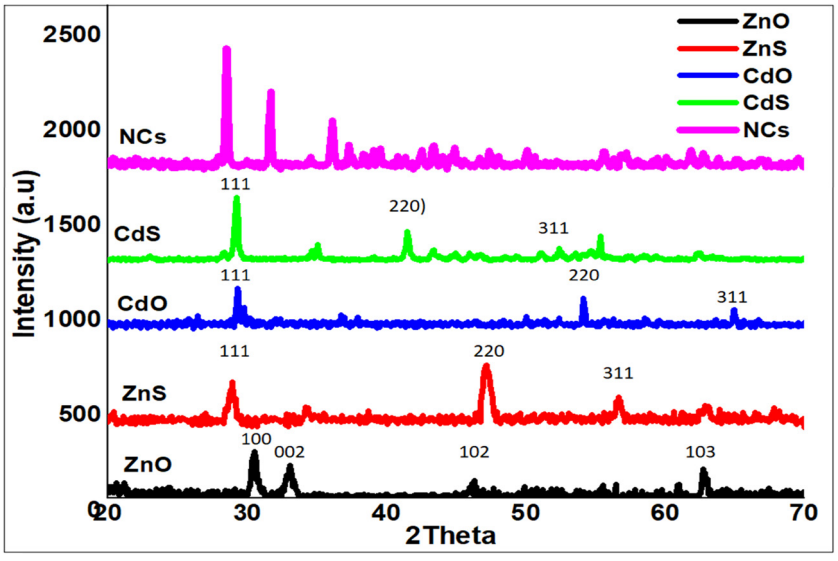

Figure 4: XRD pattern of the synthesized NPs and NCs.

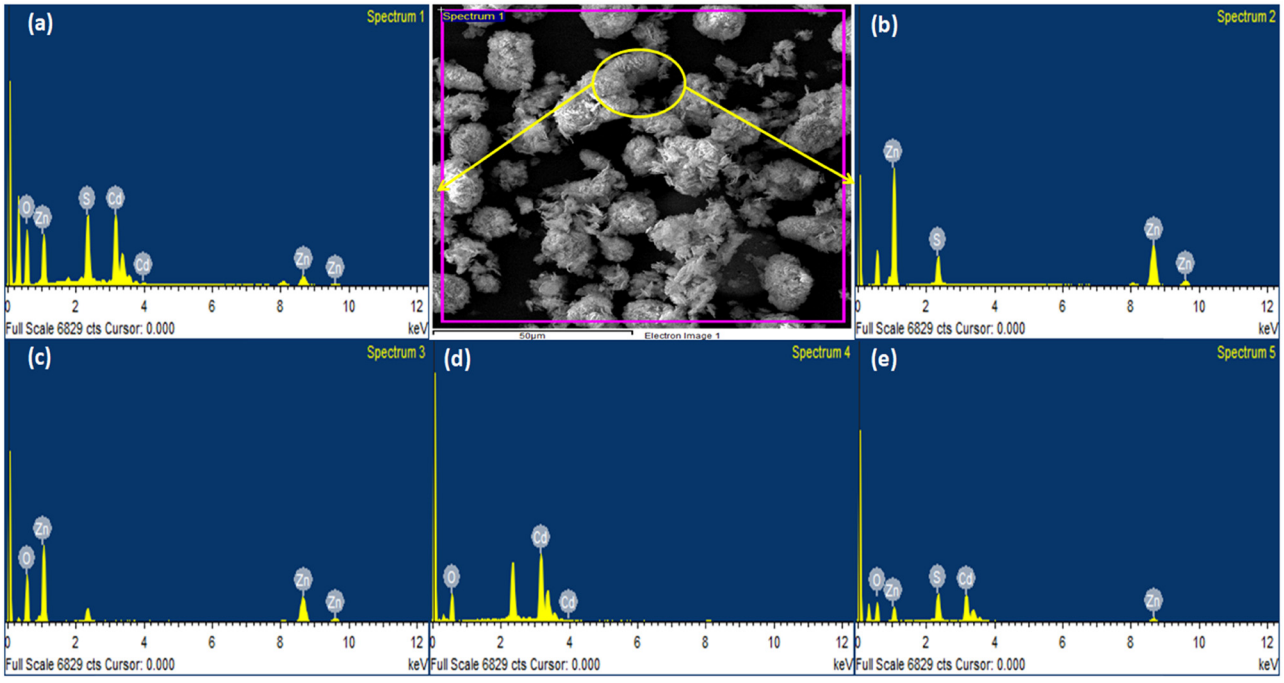

Figure 5: EDX investigation of (a) NCs, (b) ZnS NPs, (c) ZnO NPs, (d) CdO NPs, and (e) CdS NPs.

The electrical and optical characteristics of NPs and NCs are dependent on their forms [52]. SEM has been utilized by various researchers to determine the size and morphology, as well as to characterize NPs [53]. The synthesized ZnO, ZnS, CdO, CdS NPs, and ZnO–ZnS–CdO–CdS NCs were polydistributed and spherical in shape, according to SEM analysis, and the sizes of NPs and NCs ranged from 1–10 µm up to 100 nm.

3.3 Photo-catalytic degradation of dyes

In recent years, commercial dyes like CR and MR have been successfully degraded using nanomaterials [54]. Two different azo dye solutions (CR and MR) were utilized to investigate the photo-catalytic performance of ZnO, CdO, CdS, and ZnO–ZnS–CdO–CdS NCs.

First, control studies for the two different dyes were carried out without the use of a catalyst, using only 3 mL of each dye in a cuvette. It was exposed to sunlight for varied periods of time and its spectrum was recorded using a UV-Vis spectrophotometer. Figure 4 illustrates control studies that reveal a small fraction of dye degradation, a process known as photolysis response. Figures 5–8 show a decrease in absorption intensities with time exposure, indicating photo-catalytic degradation of CR and MR dyes [55]. With increasing irradiation time, the absorbance maximum (495 nm for CR and 488 nm for MR) gradually dropped. The degradation percentage and ln C_t/C_o of all the dyes in the presence of the produced NPs and NCs are also shown in Figures 7–10. The degradation percentage of the dyes was calculated by using the following equation:

$$\text{Degradation percentage} = 100 - \left(\frac{A_t \times 100}{A_0}\right) \quad (2)$$

where A_0 represents the initial absorbance of the dye solution and A_t represents the absorbance at different intervals [56].

As evident from Figure 7, the degradation percentage of the CR dye was 83% by ZnO NPs, 71% by CdO NPs, 68% by CdS NPs, and 86% by the prepared NCs.

In the case of MR degradation, the degradation percentage was 82% by ZnO NPs, 97% by CdO NPs, 77% by CdS NPs, and 93% by the prepared NCs (Figure 9).

It is noteworthy that the prepared NCs had the maximum efficiency in the case of CR and noticeable efficiency in the case of MR.

3.3.1 Kinetics of photodegradation

We can understand dye degradation behaviors using the Langmuir–Hinshelwood (L–H) model. Therefore, the pseudo-first-order equation can be expressed as follows:

$$\text{Rate}(r) = dc/dt = \ln(C_t/C_0) = -k_{app}t \quad (3)$$

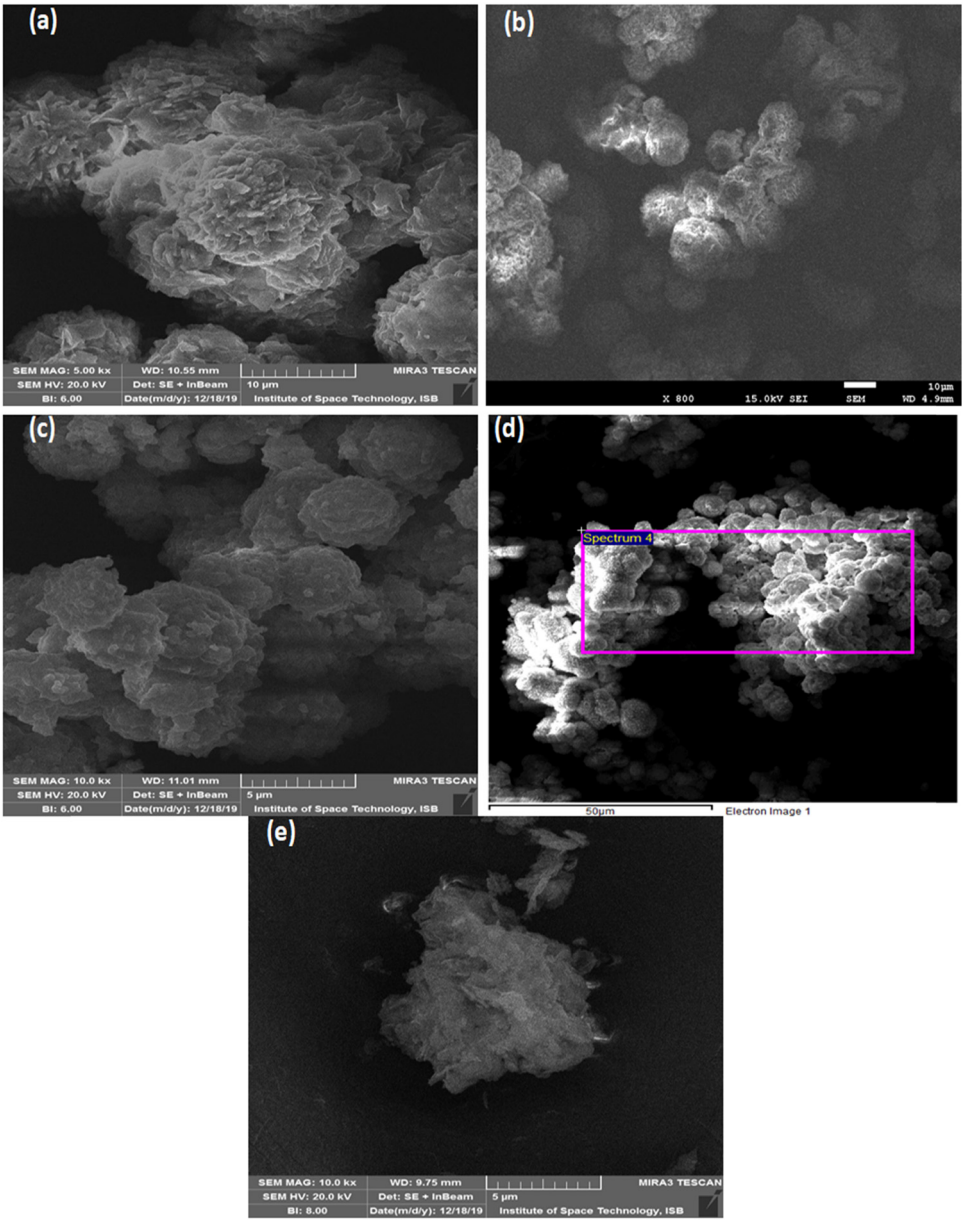

Figure 6: SEM analysis of (a) NCs, (b) ZnS NPs, (c) ZnO NPs, (d) CdO NPs, and (e) CdS NPs.

Since the reaction is colored, the rate of reaction can be determined and expressed in adsorption spectra at time t:

$$\text{Rate}(r) = \ln(C_t/C_0) = \ln(A_t/A_0) = -k_{app}t \quad (4)$$

where C_o is the initial concentration and C_t is the final concentration.

The half-life ($t_{½}$) is calculated from Eq. 5 as

$$\text{Half} - \text{life}(t_{½}) = 0.69/k \quad (5)$$

where C_0 is the initial concentration and C_t is the concentration at time (t) of the dye.

Figures A2 and A3 show a linear relationship in plots of ln (C_t/C_0) versus time of degradation. So, the degradation of dyes followed the first-order kinetics. From Eq. 5, the slopes of $\ln(C_t/C_0)$ vs time and half-life ($t_{1/2}$) of the degraded dye samples were calculated (in min) in the presence of ZnO, CdO, CdS NPs, and ZnO–ZnS–CdO–CdS NCs for CR and MR dyes, respectively [57,58].

The slope and half lifetime for CR dyes were 0.1112 and 6.2 in the presence of ZnO, 1.11 and 0.62 for CdO, 0.1335 and 5.16 for CdS, and 0.2425 and 2.85 for oil NCs, respectively. Similarly, for MR dyes, the slope and half lifetime were 0.4129 and 1.67 for ZnO, 0.9021 and 0.76 for

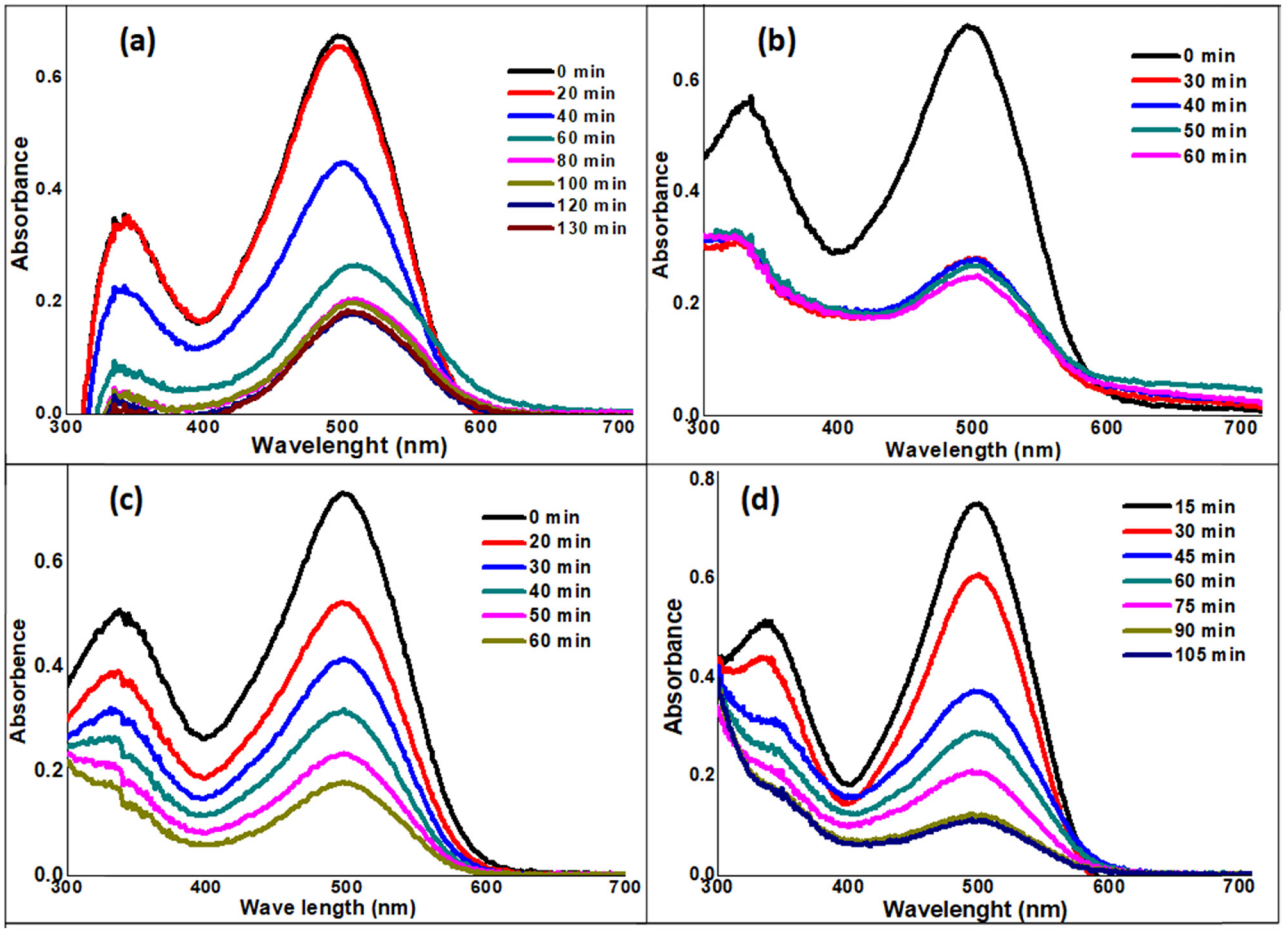

Figure 7: UV-Vis spectra of the CR dye degradation in the presence of (a) ZnO, (b) CdO, (c) CdS, and (d) NCs.

CdO, 0.2231 and 3.10 for CdS, and 0.2231 and 3.10 for oil NCs, respectively.

Thus, the above kinetic study exposed that ZnO–ZnS–CdO–CdS NPs and NCs are efficient photo-catalysts for the removal of the given dyes. The synthesized NCs showed the highest efficiency for the degradation CR dyes and a well-defined result for MR. CR was chosen for further investigation because it had the highest efficiency when compared to MR.

3.3.2 Degradation of a mixture of MR and CR

In order to check the catalytic degradation activity of the prepared NCs, the catalyst was tested in this work against a solution of a mixture of dyes. For the degradation of the mixed solution of MR and CR, 25 mL of each 0.04 mM dye was mixed in a reaction beaker. Then, 50 mg of NCs was added into the reaction vessel, and its spectra were recorded using a UV-Vis spectrophotometer. The reaction mixture was placed under a magnetic stirrer in solar light. The spectra of the solution mixture were then recorded using a UV-Vis spectrophotometer. A strong absorption peak is observed at 491 nm for the aqueous MR and CR mixture, as shown in Figure A4.

It is well known that an absorption peak is observed at 495 nm for CR, while that of MR is observed at 488 nm. Thus, the appearance of the peak at 491 nm was due to the chemical interaction of the two dye solutions. The peak intensity at 491 nm decreases after the addition of 10 mg of the catalyst in sunlight. UV-Vis spectra were continuously recorded at a time interval of 15 min, as shown in Figure A4. With time, the intensity of the peak decreases at 491 nm. The decrease in the peak intensity at 491 nm after the addition of the catalyst was due to the initiation of dye degradation [59,60]. The prepared NCs show excellent catalytic degradation activity, and the 74% degradation of the mixture of CR and MR takes 105 min. Thus, the prepared NC catalyst has the best catalytic degradation activity not only for a single substrate but also for a mixture of dyes.

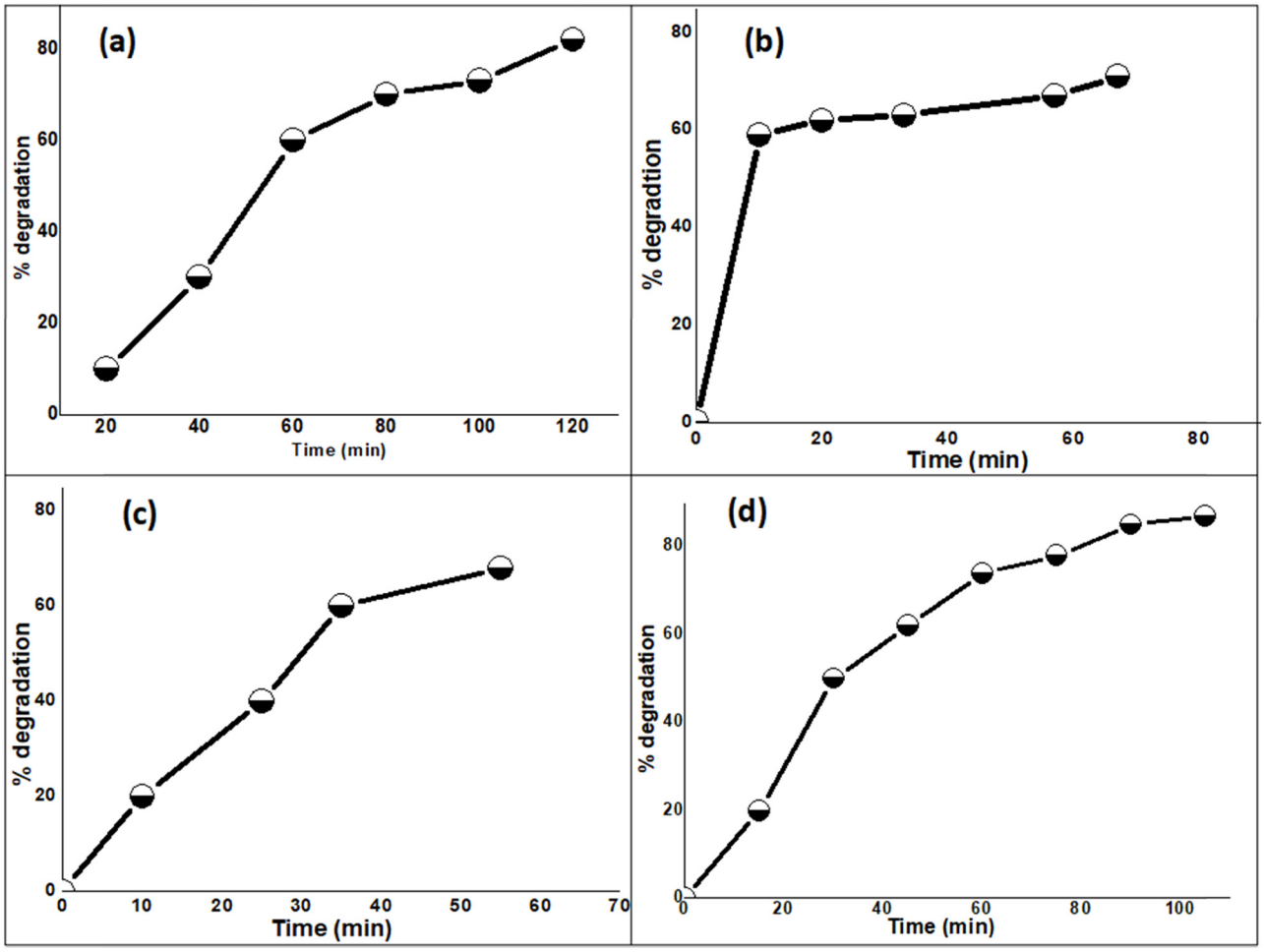

Figure 8: Degradation percentage of the CR dye: (a) ZnO, (b) CdO, (c) CdS, and (d) NCs.

3.3.3 Reusability of NCs

The reusability of effective catalysts and their uses for the next cycle is a major concern in catalysis. The majority of catalysts are deactivated after just one or two cycles of usage. In addition to catalytic efficiency, other important factors to take into account when assessing catalysts' performance include photocorrosion, versatility, compostability, and stability since they may significantly lower the overall expenses of the process [61]. Heterogeneous NP-based catalysts have been effectively documented in the literature due to their photocatalytic activity; however, the problem is that they must recover from the reaction media in order to be reused. Thus, stable and fully separable catalysts are essential to the processes of recycling and reuse.

The recyclability of catalysts was investigated using CR in this study. The degradation of CR was evaluated for 105 min for consecutive three cycles. The recyclability was tested after washing the catalyst three times in double distilled water when it was used for degradation and utilized for the next reaction at the same time.

As shown in Figure A5, ZnO degrades the CR dye by 83%, 75%, and 71% for the first, second, and third cycles, respectively. Similarly, CdO degrades the CR dye by 71%, 60%, and 65% for the first, second, and third cycles, respectively. Degradation percentage of CdS were 68%, 64%, and 59% for the first, second, and third cycles, respectively. However, degradation efficiencies of NCs were 86%, 80%, and 76% for the first, second, and third cycles, respectively.

3.3.4 Mechanism of degradation

A schematic representation of organic dye photocatalysis by the prepared NCs is illustrated in Scheme 1. It provides a plausible mechanism for the degradation reaction. The

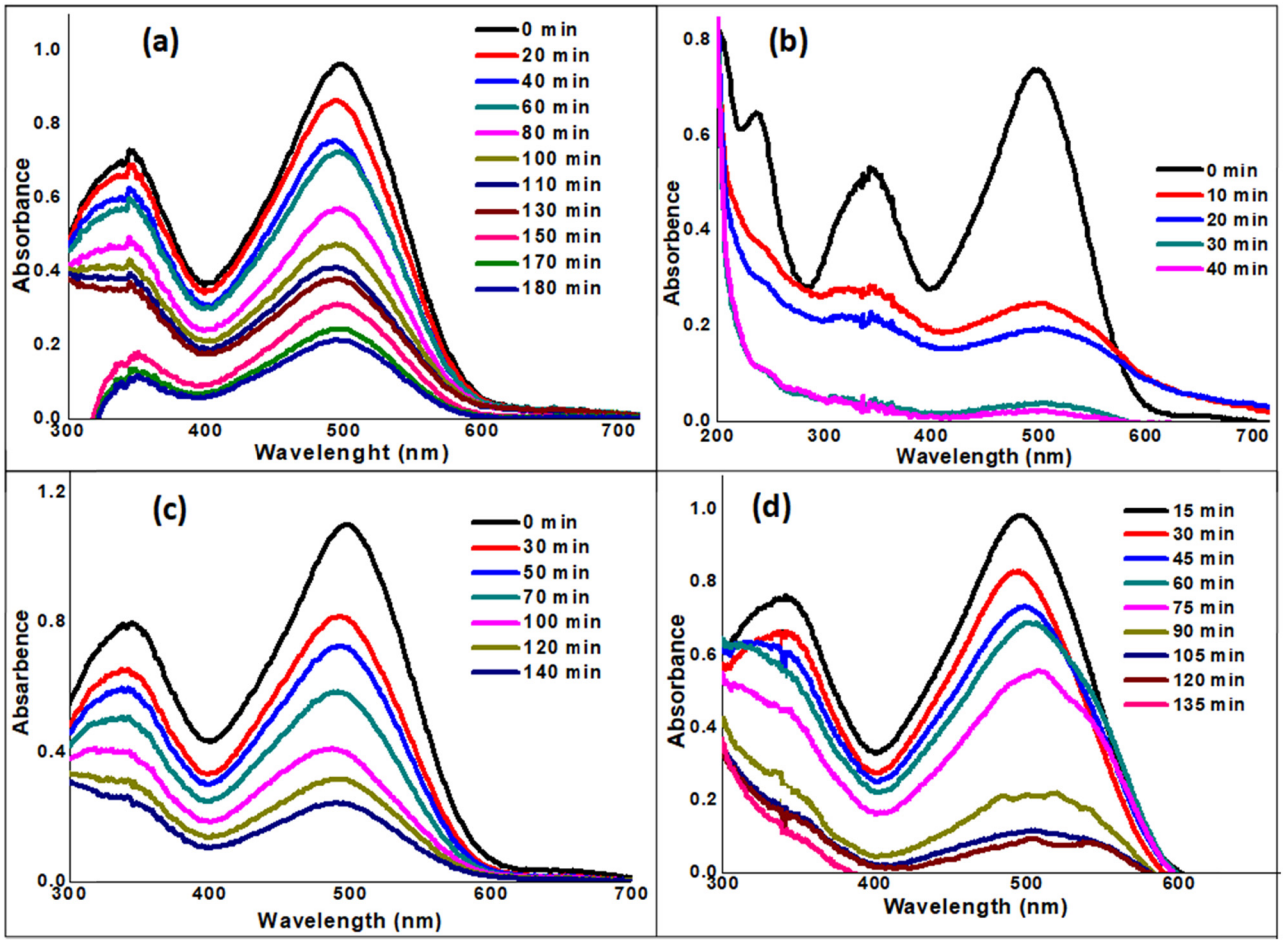

Figure 9: UV-Vis spectra of the MR dye degradation in the presence of (a) ZnO, (b) CdO, (c) CdS, and (d) NCs.

proposed degradation mechanism of the dye reaction is as follows. Photoelectrons are elevated from the valence band (VB) of the NC catalyst to the conduction band (CB), which often initiates photocatalytic activities. The energy of the absorbed light has now reached or exceeded the photocatalyst band gap energy. Photoelectron excitation causes a hole to form in the VB. As a result, a pair of electron and hole (e^-/h^+) is produced, as shown in the following equation:

$$NCs + h\nu \rightarrow NCs(e^-(CB) + h^+(VB)) \quad (6)$$

The generation of hydroxyl radicals ($OH^{\cdot}$) occurs when water ionizes and combines with the newly generated hole in the VB to produce a hydroxyl radical. This process is implicated in the destruction of the dye molecule:

$$H_2O + h^+(VB) \rightarrow OH^{\cdot}(ads) + H^+(ads) \quad (7)$$

This $OH^{\cdot}$ radical on the surface of NCs is a very potent oxidizing agent, and dye molecules that are close to the catalyst surface mineralize molecules to varying degrees depending on their structure and stability. These hydroxyl radicals can destroy any existing bacteria in the media in addition to attacking organic contaminants [62]. Similarly, the excited electrons in the conducting band now interact with the oxygen in the area to generate the anionic superoxide radical (O_2^-) at the same time:

$$O_2 + e^-(CB) \rightarrow O_2^-(ads) \quad (8)$$

Superoxide radicals contribute to the oxidation process while also preventing electron and hole recombination, preserving electron neutrality inside the catalyst.

Superoxide is protonated in this step, which results in the production of H_2O_2. This further splits apart and produces a hydroxyl radical, which is very reactive. The oxidation and reduction processes occur at the same time on the photo-excited catalyst surface in photo-catalysis. Scheme 1 shows the procedure and plausible mechanism of dye degradation.

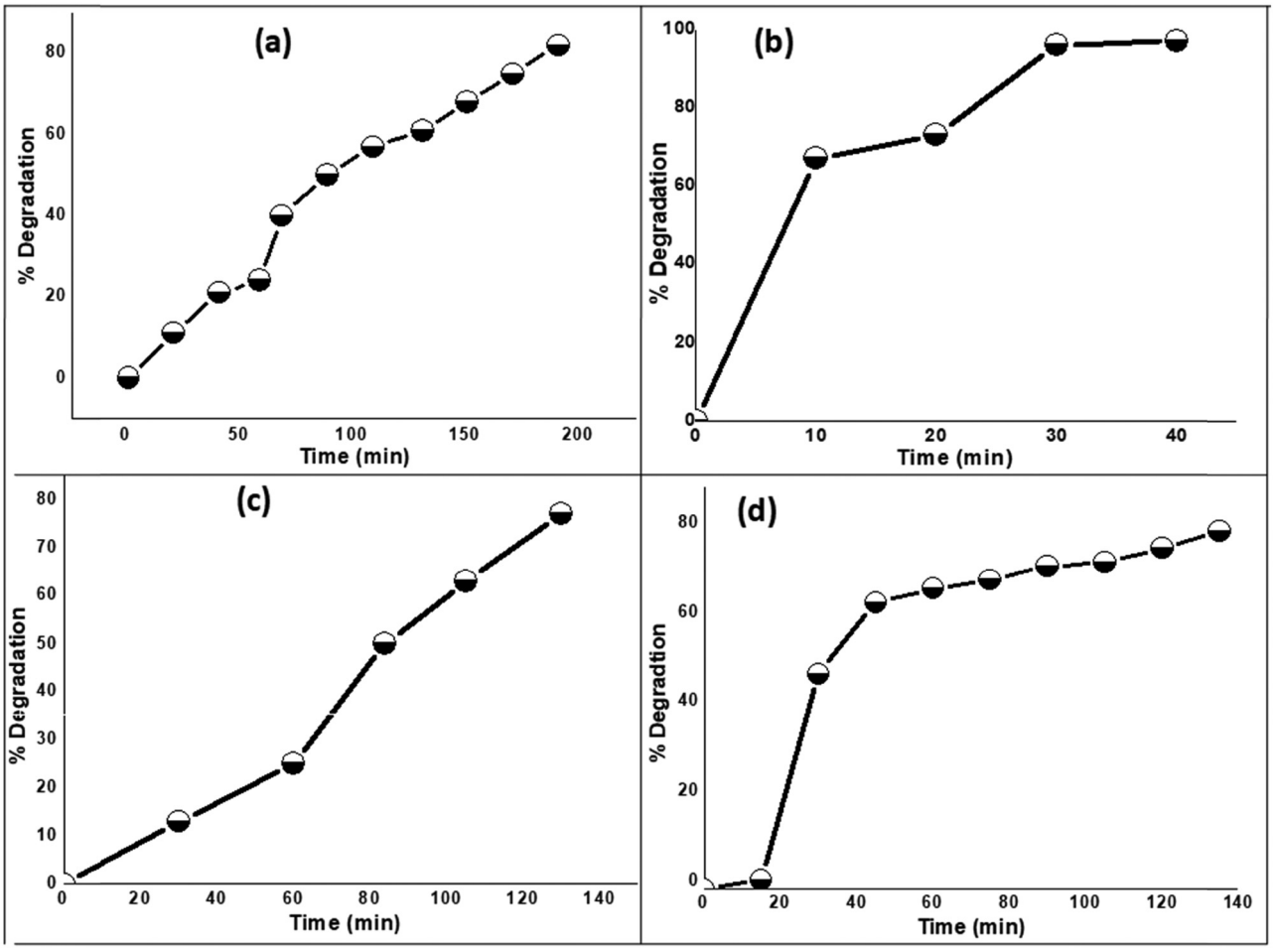

Figure 10: Degradation percentage of the MR dye: (a) ZnO, (b) CdO, (c) CdS, and (d) NCs.

3.4 Hydrogen gas generation from the biomass

The prepared nanocatalysts were used in the production of hydrogen gas from green sources of the *Brassica campestris* leaf extract. Hydrogen produced through gasification exhibits an economic efficiency compared to other renewable energy sources.

3.4.1 Gas generation from the biomass using ZnO NPs

The experiment for gas generation from the biomass was carried out in a round bottom flask used as a reaction container as presented in Figure A5, where in each case 100 W tungsten lamp is used as a source of radiation. In the absence of the prepared catalyst, the flask was filled with only 10 mL of 0.05 M KOH solution. Through rubber tubing, the flask was connected to a 500 mL graduating cylinder. The flask was placed on the magnetic stirrer to be stirred. The entire assembly was placed in a tungsten lamp, and the gas production was measured. After 1 h, 91 $\mu mol \cdot g^{-1} \cdot min^{-1}$ gas was generated. In another trial, 10 mL of the biomass extract alone was added, and 122 $\mu mol \cdot g^{-1} \cdot min^{-1}$ gas was generated in 1 h.

Similarly, in the presence of a catalyst, the round bottom flask was filled with 20 mL of the biomass extract and then 20 mg of ZnO NPs was added. The process was initiated and gas production started, and produced 550 $\mu mol \cdot g^{-1} \cdot min^{-1}$. The amount of the biomass extract was constant at 20 mL, while the catalyst amount increased from 20 to 50 mg. With an increase in the amount of catalyst, the gas production increased from 550 to 672 $\mu mol \cdot g^{-1} \cdot min^{-1}$ in 1 h (Figure 11a and b).

In order to increase H_2 production, Reddy et al. have shown that sodium hydroxide can be utilized as an effective additive in glucose gasification and the supercritical water reaction of cellulose [63]. At a comparatively low temperature of 573 K, Ishida et al. showed that the addition of sodium hydroxide could greatly increase the H_2

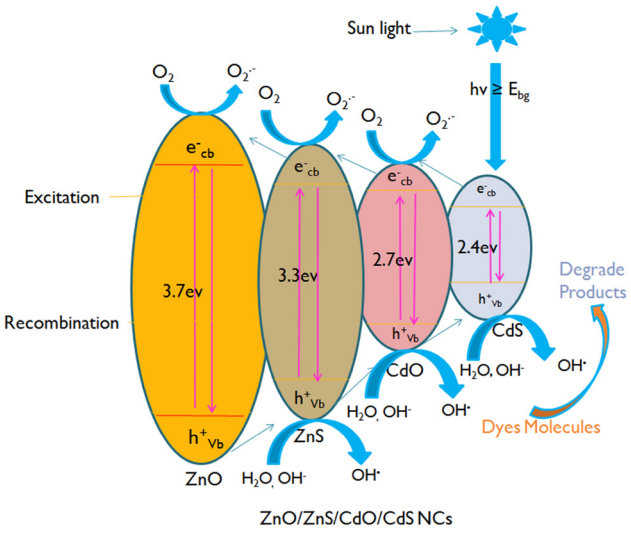

Scheme 1: Possible mechanism of photodegradation of the dye for ZnO/ZnS/CdO/CdS NCs.

output from cellulose [64]. They proposed the following alkaline thermal treatment reaction stoichiometry:

$$C_6H_{10}O_5(s) + 12NaOH(s) + H_2O(g) \rightarrow 6Na_2CO_3(s) + 12H_2(g) \quad (9)$$

Sodium hydroxide's effectiveness in generating H_2 is due to its capacity to promote the dissolving of cellulose [65] and the disintegration of cellulose [66]. Additionally, the solid carbonate formed during this reaction traps the carbon dioxide formed during it, producing H_2 with little to no carbon dioxide. The hydroxyl group may enable H_2 synthesis from cellulose at lower pressures and temperatures according to a comparison of the literature regarding the supercritical water reaction with sodium hydroxide and alkaline thermal treatment reaction [67].

The mechanisms of photo-electrochemical hydrogen production from the biomass (presented as $C_xH_yO_z$) and water over prepared NCs are shown in Eqs. 10–13. Under

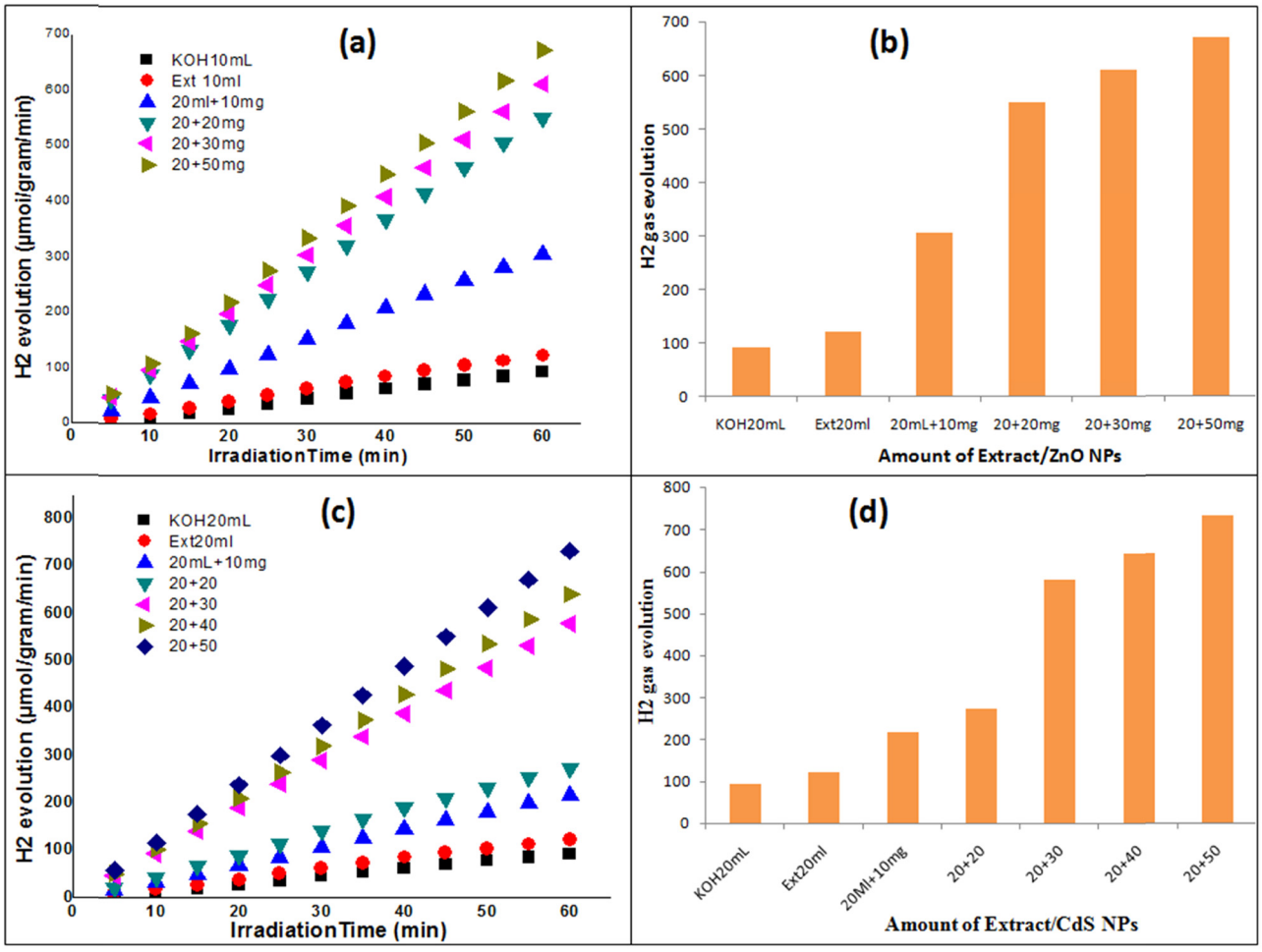

Figure 11: (a) H_2 generation in the presence of ZnO NPs. (b) The rate of H_2 evolution with various amounts of ZnO NPs. (c) H_2 generation in the presence of CdS NPs. (d) The rate of H_2 evolution with various amounts of CdS NPs. (From 10 mL 0.05 M KOH, 10 mL biomass extract, 20 mL biomass + 10 mg NPs, 20 mL biomass + 20 mg NPs, 30 mg NPs, and 20 mL biomass + 50 mg NPs, 60 min at 100 W tungsten lamp, respectively).

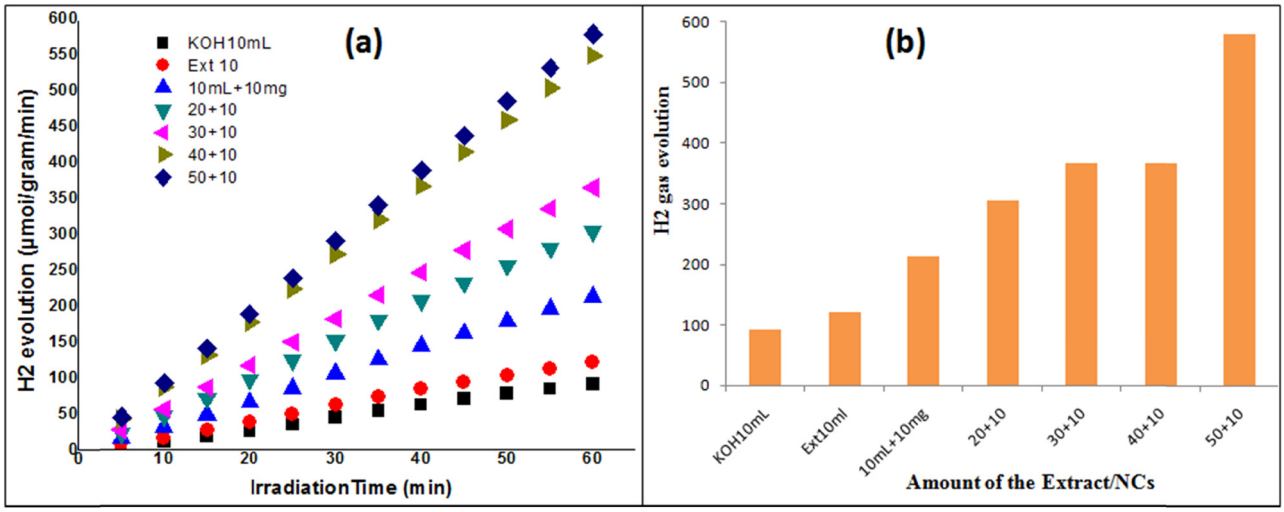

Figure 12: (a) H_2 generation from the biomass in the presence of oil NCs and NPs. (b) The rate of H_2 evolution with various amounts of oil NCs.

irradiation with sunlight (photon energy), the electrons (e^-) from the VB will be excited and transferred to the CB, and then finally react with a proton (H^+) to produce hydrogen gas. Photo-excited h^+ generated in the VB of the NCs will oxidize the $C_xH_yO_z$ molecules to carbon dioxide and water. In actuality, the process by which $C_xH_yO_z$ degrades into CO_2 and water is incredibly complicated, as explored in more detail below. The following equations succinctly describe the chemical processes [68]:

$$\text{CdS or ZnO or NCs} + h\nu \rightarrow \text{CdS}^\star \text{ or ZnO}^\star \text{ or NCs}^\star + e^- + h^+ \quad (10)$$

$$C_xH_yO_z + (4x + y - 2z)h^+ + (4x + y - 2z)OH^- \rightarrow xCO_2 + (2x + y - z)H_2O \quad (11)$$

$$2H_2O + 2e^- \rightarrow H_2 + 2OH^- \quad (12)$$

$$\text{Total: } C_xH_yO_z + (2x - z)H_2O^- \rightarrow xCO_2 + (2x - z + (y/2))H_2 \quad (13)$$

3.4.2 Gas generation from the biomass by using CdS NPs

About 20 mL of the biomass extract prepared in 0.05 M KOH solution and 10 mg of CdS NPs were taken in a round bottom flask. The reaction was started; 216 µmol·g^{-1}·min^{-1} H_2 gas was collected in the graduated cylinder. Then, the amount of the biomass extract was kept constant at 20 mL, while the amount of the photo-catalyst was changed to 20, 30, 40, to 50 mg. The H_2 gas concentrations collected were 274, 580, 641, and 733 µmol·g^{-1}·min^{-1}, respectively, in 60 min, while the rate of H_2 evolution is shown in Figure 11c and d.

3.4.3 Hydrogen gas generation from the biomass by using oil NCs

About 10 mL of the biomass extract and 10 mg of oil NCs were taken in a round bottom flask. The process was initiated, and the graduated cylinder was filled with 214 µmol·g^{-1}·min^{-1} H_2. The catalyst concentration was kept constant at 10 mg, and the biomass extract concentration was varied from 20 to 50 mL, resulting in H_2 gas concentrations of 305, 366, 550, and 580 µmol·g^{-1}·min^{-1}, respectively, in 60 min, as shown in Figure 12. In another experiment, the biomass value was held constant at 20 mL, while the oil NC values were adjusted to 10, 20, 30, 40, and 50 mg in that order. As shown in Figure 12, the H_2 generated was 305 µmol·g^{-1}·min^{-1} for 10 mg NCs, 397 µmol·g^{-1}·min^{-1} for 20 mg, 458 µmol·g^{-1}·min^{-1} for 30 mg, 611 µmol·g^{-1}·min^{-1} for 40 mg, and 763 µmol·g^{-1}·min^{-1} for 50 mg NCs.

4 Conclusions

In this work, quaternary NCs were successfully developed through an *in situ* precipitation method. Here, castor oil was used as a capping agent in deionized water. The synthesized pure NPs and NCs were characterized by UV-Vis, PL, FTIR, XRD, EDX, and SEM analyses to study

their optical, structural, and morphological data. UV-Vis spectroscopy showed the redshift in the NCs as compared to CdS NPs. This indicates the presence of more CdS NPs in NCs and hence exhibits better visible light photo-catalytic activity. PL spectroscopy reveals evidence for interaction between ZnO, ZnS, CdO, and CdS. The photo-catalytic properties of NCs and hydrogen gas generation are encouraging as compared to pure ZnO, ZnS, CdO, and CdS NPs due to efficient charge separation in ZnO–ZnS–CdO–CdS NCs.

Acknowledgements: This study is based on the work conducted by Mr. Yousaf Khan as part of his PhD thesis under the supervision of Prof. Dr. M. I. Khan and Prof. Dr. Murad Ali Khan.

Author contributions: Yousaf Khan, Uzma Sharafat, Rafia Younus, Saima Gul: conceptualization, investigation, formal analysis, methodology, visualization, and validation; Murad Ali Khan, Muhammad Ismail: formal analysis, investigation, writing – original draft, methodology, validation, writing – review and editing; Sher Bahadar Khan, M. I. Khan: project administration, visualization, supervision, resources, data curation, writing – review and editing.

Conflict of interest: The authors state that there are no conflict of interest.

Data availability statement: The authors confirm that the data supporting the findings of this study are available within the article.

References

[1] Ismail M, Akhtar K, Khan M, Kamal T, Khan MA, M Asiri A, et al. Pollution, toxicity and carcinogenicity of organic dyes and their catalytic bio-remediation. Curr Pharm Des. 2019;25(34):3645–63.

[2] Ismail M, Khan M, Khan SA, Qayum M, Khan MA, Anwar Y, et al. Green synthesis of antibacterial bimetallic Ag–Cu nanoparticles for catalytic reduction of persistent organic pollutants. J Mater Sci Mater Electron. 2018;29(24):20840–55.

[3] Al-Hamoud K, Shaik MR, Khan M, Alkhathlan HZ, Adil SF, Kuniyil M, et al. Pulicaria undulata extract-mediated eco-friendly preparation of tio2 nanoparticles for photocatalytic degradation of methylene blue and methyl orange. ACS Omega. 2022;7(6):4812–20.

[4] Khan SA, Ismail M, Anwar Y, Farooq A, Al Johny BO, Akhtar K, et al. A highly efficient and multifunctional biomass supporting Ag, Ni, and Cu nanoparticles through wetness impregnation for environmental remediation. Green Process Synth. 2019;8(1):309–19.

[5] Ismail M, Gul S, Khan M, Khan MA, Asiri AM, Khan SB. Medicago polymorpha-mediated antibacterial silver nanoparticles in the reduction of methyl orange. Green Process Synth. 2019;8(1):118–27.

[6] Riaz M, Sharafat U, Zahid N, Ismail M, Park J, Ahmad B, et al. Synthesis of biogenic silver nanocatalyst and their antibacterial and organic pollutants reduction ability. ACS Omega. 2022;7(17):14723–34.

[7] Bilal M, Khan S, Ali J, Ismail M, Khan MI, Asiri AM, et al. Biosynthesized silver supported catalysts for disinfection of Escherichia coli and organic pollutant from drinking water. J Mol Liq. 2019;281:295–306.

[8] Bakhsh EM, Ismail M, Sharafat U, Akhtar K, Fagieh TM, Danish EY, et al. Highly efficient and recoverable Ag-Cu bimetallic catalyst supported on taro-rhizome powder applied for nitroarenes and dyes reduction. J Mater Res Technol. 2022;18:769–87.

[9] Riaz M, Ismail M, Ahmad B, Zahid N, Jabbour G, Khan MS, et al. Characterizations and analysis of the antioxidant, antimicrobial, and dye reduction ability of green synthesized silver nanoparticles. Green Process Synth. 2020;9(1):693.

[10] Albukhari SM, Ismail M, Akhtar K, Danish EY. Catalytic reduction of nitrophenols and dyes using silver nanoparticles @ cellulose polymer paper for the resolution of waste water treatment challenges. Colloids Surf A. 2019;577:548–61.

[11] Khan SA, Rasool S, Rehman KU, Hussain S, Khan I, Ismail M, et al. A simple but efficient catalytic approach for the degradation of pollutants in aqueous media through *Cicer arietinum* supported Ni nanoparticles. Z Phys Chem. 2020;234(11–12):1789–802.

[12] Shah Z, Gul T, Khan SA, Shaheen K, Anwar Y, Suo H, et al. Synthesis of high surface area AgNPs from *Dodonaea viscosa* plant for the removal of pathogenic microbes and persistent organic pollutants. Mater Sci Eng B. 2021;263:114770.

[13] Ismail M, Gul S, Khan M, Khan MA, Asiri AM, Khan SB. Green synthesis of zerovalent copper nanoparticles for efficient reduction of toxic azo dyes Congo red and methyl orange. Green Process Synth. 2019;8(1):135–43.

[14] You H, Wu Z, Jia Y, Xu X, Xia Y, Han Z, et al. High-efficiency and mechano-/photo-bi-catalysis of piezoelectric-ZnO@ photoelectric-TiO2 core-shell nanofibers for dye decomposition. Chemosphere. 2017;183:528–35.

[15] Wang Z, Zhang H, Cao H, Wang L, Wan Z, Hao Y, et al. Facile preparation of ZnS/CdS core/shell nanotubes and their enhanced photocatalytic performance. Int J Hyd Energy. 2017;42(27):17394–402.

[16] Ayodhya D, Veerabhadram G. A review on recent advances in photodegradation of dyes using doped and heterojunction based semiconductor metal sulfide nanostructures for environmental protection. Mater Today energy. 2018;9:83–113.

[17] Tian Y, Newton T, Kotov NA, Guldi DM, Fendler JH. Coupled composite CdS– CdSe and core– shell types of (CdS) CdSe and (CdSe) CdS nanoparticles. J Phy Chem. 1996;100(21):8927–39.

[18] Lee C, Lee T, Lyu S, Zhang Y, Ruh H, Lee H. Growth mechanism and field emission properties of inject-like ZnO nanostructure. Appl Phys Lett. 2002;81:3648–50.

[19] Peng X, Wickham J, Alivisatos A. Kinetics of II-VI and III-V colloidal semiconductor nanocrystal growth:"focusing" of size distributions. J Am Chem Soc. 1998;120(21):5343–4.

[20] Thovhogi N, Park E, Manikandan E, Maaza M, Gurib-Fakim A. Physical properties of CdO nanoparticles synthesized by green chemistry via Hibiscus Sabdariffa flower extract. J Alloy Comp. 2016;655:314–20.
[21] Xi G, Peng Y, Zhu Y, Xu L, Zhang W, Yu W, et al. Preparation of β-MnO2 nanorods through a γ-MnOOH precursor route. Mater res bull. 2004;39(11):1641–8.
[22] Zhang H, Chen X, Li Z, Kou J, Yu T, Zou Z. Preparation of sensitized ZnS and its photocatalytic activity under visible light irradiation. J Phy D Appl Phy. 2007;40(21):6846.
[23] Song S, Hong F, He Z, Wang H, Xu X, Chen J. Influence of zirconium doping on the activities of zirconium and iodine co-doped titanium dioxide in the decolorization of methyl orange under visible light irradiation. Appl Surf Sci. 2011;257(23):10101–8.
[24] Macias-Sanchez S, Nava R, Hernandez-Morales V, Acosta-Silva Y, Gomez-Herrera L, Pawelec B, et al. Cd1– xZnxS solid solutions supported on ordered mesoporous silica (SBA-15): structural features and photocatalytic activity under visible light. Int J Hydr Energy. 2012;37(13):9948–58.
[25] Rao BS, Kumar BR, Reddy VR, Rao TS, Chalapathi GV. Influence on optical properties of nickel doped cadmium sulfide. Chalcogenide Lett. 2011;8(1):39–44.
[26] Wang S, Liu P, Wang X, Fu X. Homogeneously distributed CdS nanoparticles in nafion membranes: preparation, characterization, and photocatalytic properties. Langmuir. 2005;21(25):11969–73.
[27] Shi J-W, Yan X, Cui H-J, Zong X, Fu M-L, Chen S, et al. Low-temperature synthesis of CdS/TiO2 composite photocatalysts: influence of synthetic procedure on photocatalytic activity under visible light. J Mol Catal A Chem. 2012;356:53–60.
[28] Reiss P, Protiere M, Li L. Core/shell semiconductor nanocrystals. Small. 2009;5(2):154–68.
[29] Sailaja AK, Amareshwar P, Chakravarty P. Different techniques used for the preparation of nanoparticles using natural polymers and their application. Int J Pharm Pharm Sci. 2011;3(2):45–50.
[30] Uddin MN, Daud WW, Abbas HF. Effects of pyrolysis parameters on hydrogen formations from biomass: a review. Rsc Adv. 2014;4(21):10467–90.
[31] Stonor MR, Ferguson TE, Chen JG, Park A-HA. Biomass conversion to H 2 with substantially suppressed CO 2 formation in the presence of Group I & Group II hydroxides and a Ni/ZrO 2 catalyst. Energy Env Sci. 2015;8(6):1702–6.
[32] Karimi Andeani J, Mohsenzadeh S. Phytosynthesis of cadmium oxide nanoparticles from *Achillea wilhelmsii* flowers. J Chem. 2013;2013:147613.
[33] Ahmed AAA, Issa SA, Al-Marbie SA, Al-Geraei MA, Al-Mtouakell HA, Al-Mangathi SA, et al. Structural, optical and antibacterial characteristics of CdO nanostructure prepared via simple method. Albaydha Univ J. 2020;2:16–24.
[34] Navakoteswara Rao V, Preethi V, Bhargav U, Ravi P, Kumar A, Sathish M, et al. Gram-scale synthesis of ZnS/NiO core-shell hierarchical nanostructures and their enhanced H2 production in crude glycerol and sulphide wastewater. Env Res. 2021;199:111323.
[35] Koutavarapu R, Reddy CV, Syed K, Reddy KR, Saleh TA, Lee D-Y, et al. Novel Z-scheme binary zinc tungsten oxide/nickel ferrite nanohybrids for photocatalytic reduction of chromium (Cr (VI)), photoelectrochemical water splitting and degradation of toxic organic pollutants. J Hazard Mater. 2022;423:127044.
[36] Taufik A, Tju H, Prakoso S, Saleh R, editors. Different routes of synthesized CdO nanoparticles through microwave-assisted methods and photocatalytic study. AIP Conference Proceedings. AIP Publishing LLC; 2018.
[37] Lavand AB, Malghe YS. Visible light photocatalytic degradation of 4-chlorophenol using C/ZnO/CdS nanocomposite. J Saudi Chem Soci. 2015;19(5):471–8.
[38] Ismail M, Khan MI, Akhtar K, Khan MA, Asiri AM, Khan SB. Biosynthesis of silver nanoparticles: A colorimetric optical sensor for detection of hexavalent chromium and ammonia in aqueous solution. Phys E: Low-dimensional Syst Nanostruct. 2018;103:367–76.
[39] Ismail M, Khan MI, Akhtar K, Seo J, Khan MA, Asiri AM, et al. Phytosynthesis of silver nanoparticles; naked eye cellulose filter paper dual mechanism sensor for mercury ions and ammonia in aqueous solution. J Mater Sci Mater Electron. 2019;30(8):7367–83.
[40] Othman A, Osman M, Wahdan M, Abed-ElRahim A. Thermal annealing and UV induced effects on the structural and optical properties of capping free ZnS nanoparticles synthesized by Co-precipitation method. Int J Gen Eng Technol. 2014;3(9):16.
[41] Rahman MM, Khan SB, Marwani HM, Asiri AM, Alamry KA, Rub MA, et al. Facile synthesis of doped ZnO-CdO nanoblocks as solid-phase adsorbent and efficient solar photo-catalyst applications. J Ind Engin Chem. 2014;20(4):2278–86.
[42] Khan Y, Gul S, Ismail M, Khan MI, Khan MA. Microwave assisted green synthesis of photoluminescent pure and mn-doped cadmium sulfide nanoparticles. J Non-Oxide Glasses. 2017;9(3):75–83.
[43] Dumbrava A, Berger D, Prodan G, Moscalu F. Functionalized Zno/Cds composites: synthesis, characterization and photocatalytic applications. Chalcogenide Lett. 2016;13(3):105–15.
[44] Zak AK, Majid WA, Abrishami ME, Yousefi R. X-ray analysis of ZnO nanoparticles by Williamson–Hall and size–strain plot methods. Solid State Sci. 2011;13(1):251–6.
[45] Pawar R. Structural and optical properties of chemically synthesized ZnS nanoparticals. Orient J Chem. 2013;29(3):1139–42.
[46] Khan SB, Ismail M, Bakhsh EM, Asiri AM. Design of simple and efficient metal nanoparticles templated on ZnO-chitosan coated textile cotton towards the catalytic reduction of organic pollutants. J Ind Text. 2022;51(1S):1703S–28S.
[47] Din A, Khan SB, Khan MI, Asif SAB, Khan MA, Gul S, et al. Cadmium oxide based efficient electrocatalyst for hydrogen peroxide sensing and water oxidation. J Mater Sci Mater Electron. 2017;28(1):1092–100.
[48] Fang D, Zhang Z, Wang Z, Ding Z. Study of photoluminescence of CdS/ZnS core/shell quantum dots. Phys Procedia. 2012;32:920–5.
[49] Murugadoss G. Structural and optical properties of monodispersed ZnS/CdS/ZnO and ZnO/ZnS/CdS nanoparticles. J Lumin. 2012;132(10):2665–9.
[50] Vanheusden K, Warren W, Seager C, Tallant D, Voigt J, Gnade B. Mechanisms behind green photoluminescence in ZnO phosphor powders. J Appl Phy. 1996;79(10):7983–90.
[51] Basavaraja S, Balaji S, Lagashetty A, Rajasab A, Venkataraman A. Extracellular biosynthesis of silver

nanoparticles using the fungus Fusarium semitectum. Mater Res Bull. 2008;43(5):1164–70.
[52] Yadav RS, Mishra R, Pandey AC. Particle size distribution study by small-angle X-ray scattering technique and photoluminescence property of ZnO nanoparticles. J Exp Nanosci. 2009;4(2):139–46.
[53] Barman J, Borah J, Sarma K. Effect of pH variation on size and structure of CdS nanocrystalline thin films. Chalcogenide Lett. 2008;5(11):265–71.
[54] Anjum F, Asiri AM, Khan MA, Khan MI, Khan SB, Akhtar K, et al. Photo-degradation, thermodynamic and kinetic study of carcinogenic dyes via zinc oxide/graphene oxide nanocomposites. J Mater Res Technol. 2021;15:3171–91.
[55] Mohapatra L, Parida K. Zn–Cr layered double hydroxide: visible light responsive photocatalyst for photocatalytic degradation of organic pollutants. Sep Purifi Technol. 2012;91:73–80.
[56] Ismail M, Khan M, Khan SB, Akhtar K, Khan MA, Asiri AM. Catalytic reduction of picric acid, nitrophenols and organic azo dyes via green synthesized plant supported Ag nanoparticles. J Mol Liq. 2018;268:87–101.
[57] Asif SAB, Khan SB, Asiri AM. Visible light functioning photocatalyst based on Al 2 O 3 doped Mn 3 O 4 nanomaterial for the degradation of organic toxin. Nanoscale Res Lett. 2015;10(1):355.
[58] Asif SAB, Khan SB, Asiri AM. Efficient solar photocatalyst based on cobalt oxide/iron oxide composite nanofibers for the detoxification of organic pollutants. Nanoscale Res Lett. 2014;9(1):1–9.
[59] Ismail M, Khan MI, Khan SB, Khan MA, Akhtar K, Asiri AM. Green synthesis of plant supported CuAg and CuNi bimetallic nanoparticles in the reduction of nitrophenols and organic dyes for water treatment. J Mol Liq. 2018;260:78–91.
[60] Ismail M, Khan MI, Khan MA, Akhtar K, Asiri AM, Khan SB. Plant-supported silver nanoparticles: Efficient, economically viable and easily recoverable catalyst for the reduction of organic pollutants. Appl Organomet Chem. 2019;33(8):e4971.
[61] Rehman AU, Sharafat U, Gul S, Khan MA, Khan SB, Ismail M, et al. Green synthesis of manganese-doped superparamagnetic iron oxide nanoparticles for the effective removal of Pb(ii) from aqueous solutions. Green Process Synth. 2022;11(1):287–305.
[62] Saien J, Soleymani AR. Feasibility of using a slurry falling film photo-reactor for individual and hybridized AOPs. J Ind Engin Chem. 2012;18(5):1683–8.
[63] Reddy SN, Nanda S, Dalai AK, Kozinski JA. Supercritical water gasification of biomass for hydrogen production. Int J Hydrog Energy. 2014;39(13):6912–26.
[64] Ishida M, Otsuka K, Takenaka S, Yamanaka I. One-step production of CO-and CO2-free hydrogen from biomass. J Chem Technol Biotechnol Int Res Process Environ Clean Technol. 2005;80(3):281–4.
[65] Isogai A, Atalla R. Dissolution of cellulose in aqueous NaOH solutions. Cellulose. 1998;5(4):309–19.
[66] Machell G, Richards G. 384. Mechanism of saccharinic acid formation. Part I. Competing reactions in the alkaline degradation of 4-O-methyl-D-glucose, maltose, amylose, and cellulose. J Chem Soci (Resumed). 1960;1924–31.
[67] Ferguson TE, Park Y, Petit C, Park A-HA. Novel approach to hydrogen production with suppressed CO x generation from a model biomass feedstock. Energy Fuels. 2012;26(7):4486–96.
[68] Lu X, Xie S, Yang H, Tong Y, Ji H. Photoelectrochemical hydrogen production from biomass derivatives and water. Chem Soci Rev. 2014;43(22):7581–93.

Appendix

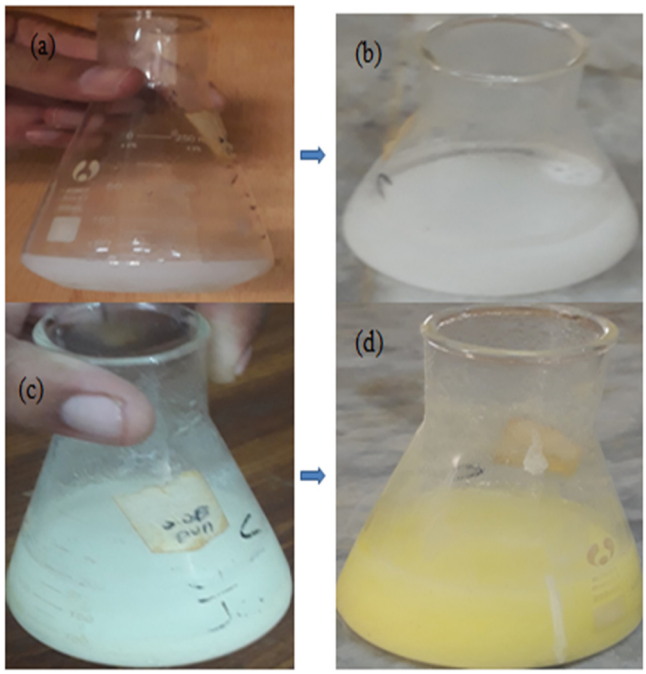

Figure A1: Synthesis of (a) ZnO NPs, (b) ZnO/ZnS NCs, (c) ZnO/ZnS/CdO NCs, and (d) ZnO/ZnS/CdO/CdS NCs.

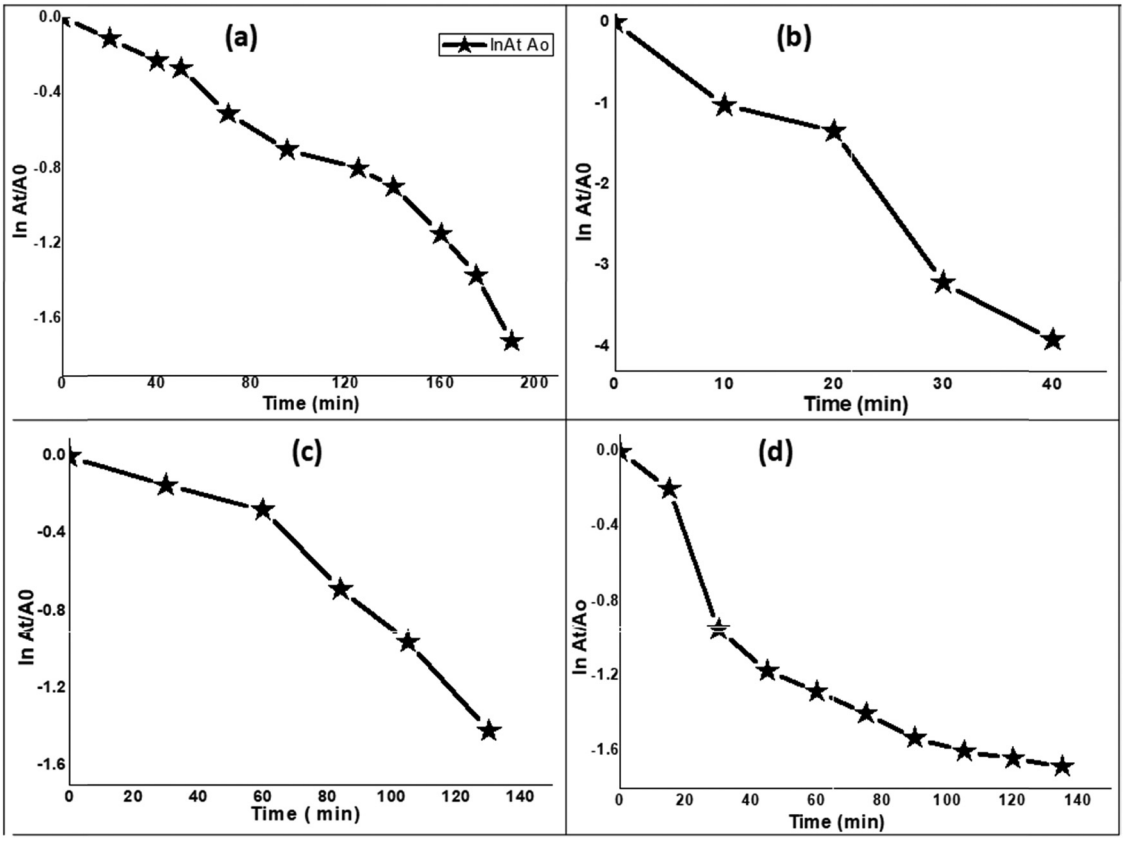

Figure A2: Plot of $\ln(C_t/C_o)$ versus time for the CR dye for (a) ZnO, (b) CdO (c), CdS, and (d) NCs.

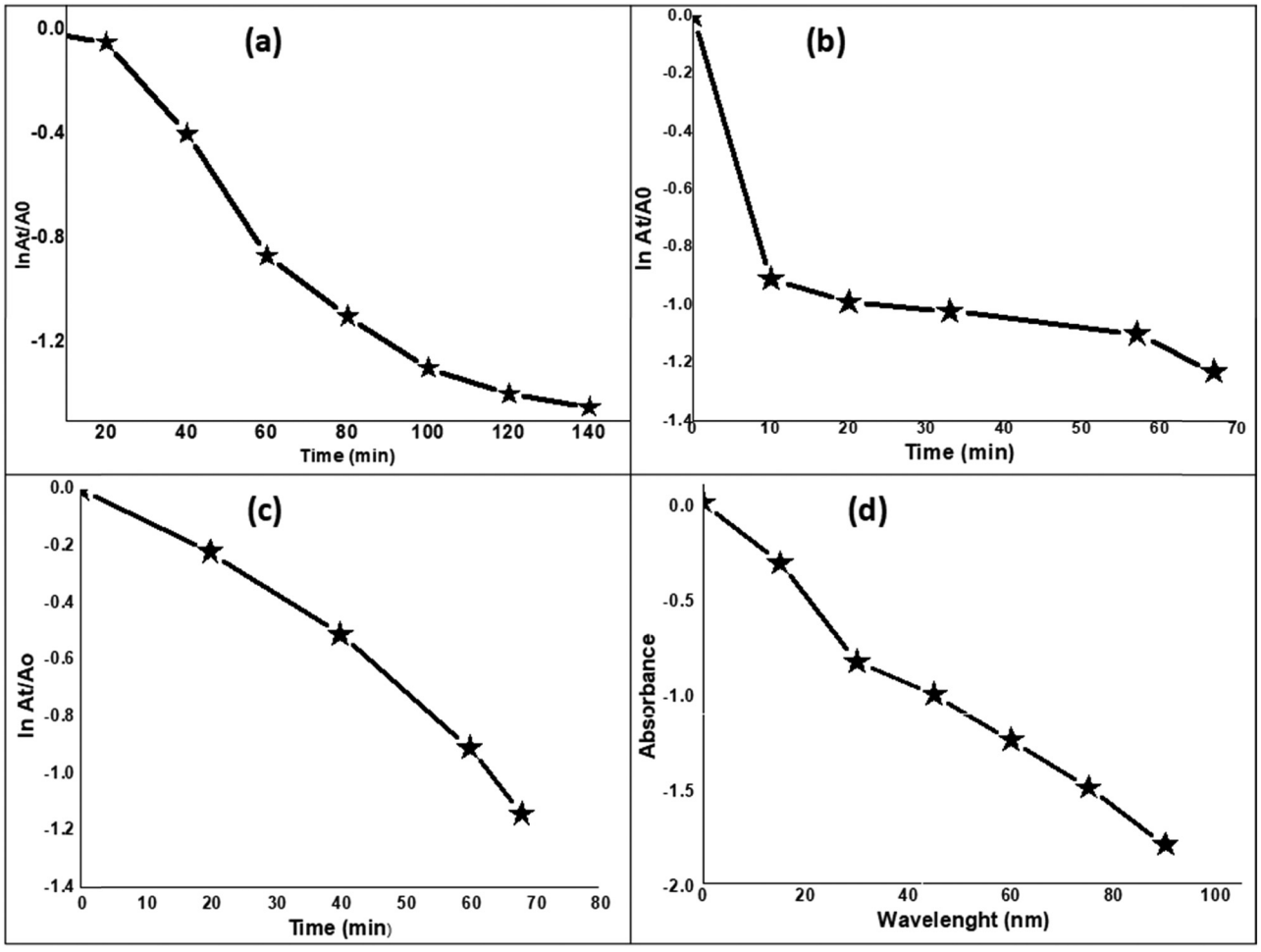

Figure A3: Plot of $\ln(C_t/C_o)$ versus time for the MR dye for (a) ZnO, (b) CdO, (c) CdS, and (d) NCs.

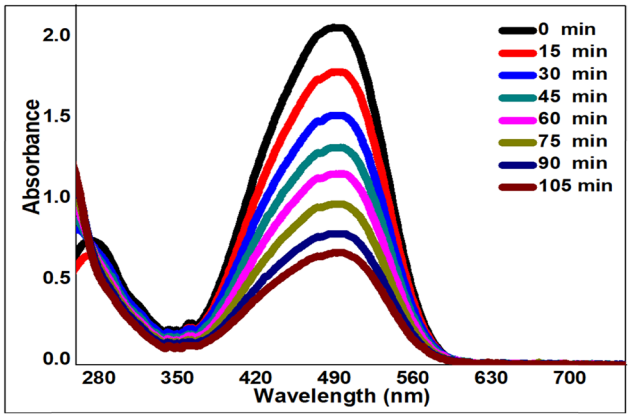

Figure A4: Photocatalytic degradation of a mixture of MR and CR dyes (25 mL of each 0.04 mM dye + 50 mg of NCs).

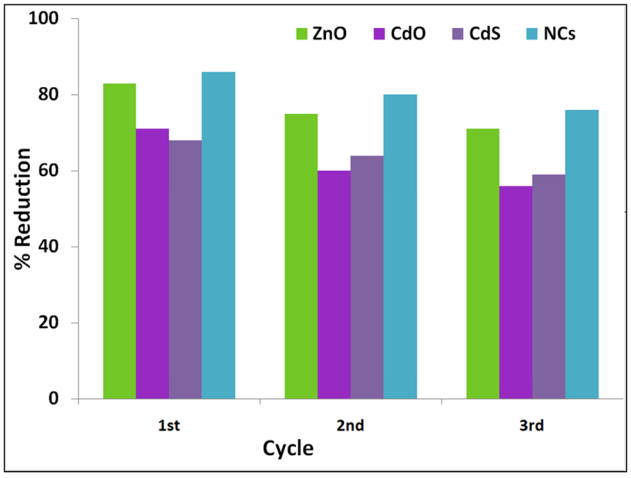

Figure A5: Reusability of the CR dye for ZnO, CdO, CdS, and NCs.

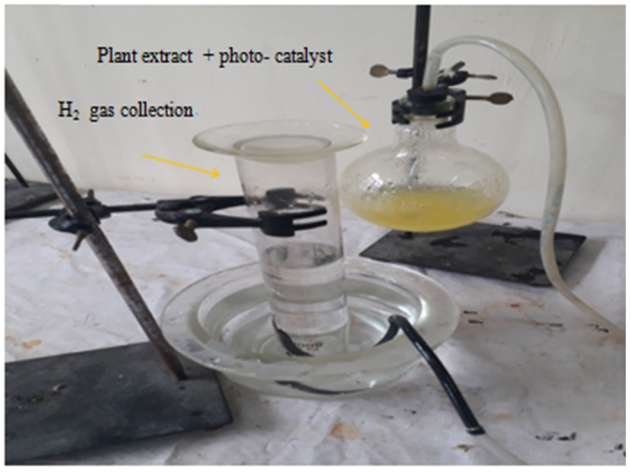

Figure A6: Set up for hydrogen generation from the biomass and photo-catalyst reaction.